Journal of the Taiwan Institute of Chemical Engineers 161 (2024) 105536

Contents lists available at ScienceDirect

Journal of the Taiwan Institute of Chemical Engineers

journal homepage: www.journals.elsevier.com/journal-of-the-taiwan-institute-of-chemical-engineers

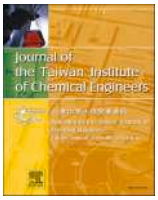

Transport and deposition of nanoparticles in porous media at the pore scale using an Eulerian-Lagrangian method

Milad Ramezanpour [a], Majid Siavashi [a,*], Hamidreza Khoshtarash [a,b], Martin J. Blunt [c]

[a] Applied Multi-phase Fluid Dynamics Laboratory, School of Mechanical Engineering, Iran University of Science and Technology, Tehran, Iran
[b] Department of Civil and Environmental Engineering, University of Houston, Houston, Texas, USA
[c] Department of Earth Science and Engineering, Imperial College London, London, SW7 2AZ, United Kingdom

ARTICLE INFO

Keywords:
Pore-scale
Nanoparticle
Lagrangian
Berea sandstone
Brownian motion
Electrostatic interactions

ABSTRACT

Background: Nanoparticle deposition in a subsurface environment decreases the amount of material in the bulk fluid, increases surface roughness, and affects nanofluid flow. Nanoparticle transport in porous media is a complex, multiscale phenomenon. Its macroscopic behavior is determined by phenomena at the pore-scale. Hence, it is necessary and of interest to study the transport and deposition of nanoparticles in porous media using a pore-scale approach.

Methods: A computational solver is developed using an Eulerian-Lagrangian approach within the OpenFOAM library. A Berea sandstone and three open-cell metal foams with porosities of 0.8, 0.85, and 0.9, constructed by Laguerre-Voronoi tessellation, were analyzed to study nanoparticle behavior in water.

Significant findings: Nanoparticle deposition on solid surfaces is influenced by porosity, double layer thickness (N_{DL}), surface potential magnitude (N_{El}), and nanoparticle diameter. Brownian motion that has a significant impact on nanoparticle transport and deposition is also examined. For nanoparticles with 20 nm diameter, the fraction of particles deposited in foam with 0.8 porosity is about 17 % more than the foam with 0.9 porosity. This difference decreases with nanoparticle diameter. For the particles with 100 nm diameter and more, the effects of Brownian motion on nanoparticle deposition becomes negligible.

1. Introduction

A nanofluid is a liquid-nanoparticle mixture with particles usually defined to be smaller than 100 nanometers in diameter. Nanofluids (a mixture of nanoparticles with Newtonian and non-Newtonian fluids) have been used in various engineering fields in recent decades [1–3]. Due to the high surface-to-volume ratio of nanoparticles, it has improved heat transfer properties compared to pure fluids in energy devices [4]. Hence, nanofluids have extensive applications in solar systems [5–7], energy devices [8,9], pharmaceutics and medicine [10] and the automotive industry [11].

Furthermore, due to their unique properties, nanofluids have extensive applications in enhanced oil recovery (EOR) [12,13]. Nanofluids can lead to EOR by various mechanisms, including the reduction of interfacial tension between water and oil, and viscosity and wettability alteration [14,15]. Moreover, deposition (sometimes called retention or attachment) of nanoparticles to the solid surface during flow in porous media is also important. For instance, subsurface colloids with a strong absorption ability carry harmful contaminants that threaten human health [16,17]. Solvents consisting of particles and fluid often have low solubility and are usually denser than water, which means that they sink and deposit at the base of aquifers, impacting the purity of groundwater for decades [18]. On the other hand, the nanofluid injection can be used to help improve oil recovery in subsurface hydrocarbon reservoirs if the deposited particles alter the surface wettability [19].

Nanoparticle transport in porous media is a multiscale and complex phenomenon. Its effects at the large scale depend on its pore-scale behavior. Pore-scale modeling of the complex interaction of structure with the multiphase flow and reactive transport has been the subject of several studies over the past few decades [20,21]. Experimentally, in the context of enhanced oil recovery, Kuang et al. [22] investigated waterflood recovery using nanofluid injection. High-resolution three-dimensional X-ray imaging was used to characterize the pore space of dolomite and Berea sandstones. Zhang et al. [23] studied oil recovery in carbonates using carbon nanosheets. The effect of nanosheets on different parameters, such as wettability alteration and interfacial tension, was

* Corresponding author.
E-mail address: msiavashi@iust.ac.ir (M. Siavashi).

https://doi.org/10.1016/j.jtice.2024.105536
Received 7 January 2024; Received in revised form 9 April 2024; Accepted 5 May 2024
Available online 11 May 2024

Nomenclature

A_H	Hammaker's constant for a spherical nanoparticle
A_i	Random numbers for Brownian motion force calculation
C_c	Cunningham slip correction factor
d_p	Nanoparticle diameter (nm)
$\boldsymbol{F}$	Force per unit mass (Nm^{-1})
$\boldsymbol{F}_B$	Buoyancy force per unit mass (Nm^{-1})
$\boldsymbol{F}_{Br}$	Brownian motion force per unit mass (Nm^{-1})
$\boldsymbol{F}_D$	Drag force per unit mass (Nm^{-1})
$\boldsymbol{F}_{EDL}$	Electrostatic double layer force per unit mass (Nm^{-1})
$\boldsymbol{F}_G$	Gravity force per unit mass (Nm^{-1})
$\boldsymbol{F}_{SL}$	Saffman lift force per unit mass (Nm^{-1})
$\boldsymbol{F}_{VDW}$	Van der Waals force per unit mass (Nm^{-1})
$\boldsymbol{F}_W$	Wall force per unit mass (Nm^{-1})
k_b	Boltzmann constant (equals $1.3806 \times 10^{-23} m^2 kg/(s^2 K)$)
Kn	Knudsen number
m	Mass (kg)
n_p	Number of nanoparticles in a computational cell
N_{E1}	Magnitude of surface potentials
N_{E2}	Ratio of surface potentials
N_{DL}	Ratio of particle radius to double layer thickness
r_p	Nanoparticle radius (nm)
S_m	Momentum transfer between the nanoparticles and fluid
T	Fluid temperature (K)
$\boldsymbol{U}$	Velocity (ms^{-1})
Z	Nearest distance between the wall surface and the nanoparticle (nm)

Greek ***Symbols***

μ	Dynamic viscosity, ($kgm^{-1}s^{-1}$)
ρ	Density, kgm^{-3}
δV	Computational cell volume, m^3
ς_i	Zero-mean, Gaussian random number
Δt	Time-step
λ	Mean free path of molecules
ψ	Surface potential
ε	Dielectric constant of the solution
κ	Inverse of the Debye-Huckel length, m^{-1}
ε_0	Permittivity of vacuum

Subscripts

f	Fluid
P	Particle
s	Solid

Acronyms

OCF	Open-cell foam
LVT	Laguerre-Voronoi tessellation
VT	Voronoi tessellation
FVM	Finite volume method
WP	Weaire–Phelan
PPI	Pores per inch
EL	Eulerian-Lagrangian
VDW	Van der Waals
EDL	Electrostatic double layer

Table 1
The properties of the OCF samples used in this study. PPI is pores per inch cubed where 1 inch is 25.4 mm, an inverse representation of the pore size.

Sample	Length (mm)	Width (mm)	Height (mm)	Pore density (PPI)	Porosity (%)
OCF-1	9.84	4.9	4.88	30	80
OCF-2	9.84	4.9	4.88	30	85
OCF-3	9.84	4.9	4.88	30	90

Table 2
The physical characteristics of the fluid and nanoparticles.

Parameter	Value
ρ_f	$998.21 kg/m^3$
ρ_p	$7870 kg/m^3$
d_p	20–100 nm
μ_f	$1.002 \times 10^{-3} kg/(m.s)$
Hammaker constant, A_H	0.4×10^{-20}
Boltzmann constant, k_B	$1.38 \times 10^{-23} J/K$
Characteristic wavelength of water, λ	100nm

investigated. Pak et al. [24] also used X-ray imaging to examine the effect of silica nanoparticles on oil removal from porous media in a pore-scale study. They concluded that nanofluid injection successfully remobilizes the trapped oil. Other applications in enhanced oil recovery include nanoparticle-assisted surfactant flooding [25], nanoparticle-stabilized microemulsions [26], and nanoparticle-stabilized foam during CO_2 injection [27].

While experiments are valuable, the complexity of the fluid systems and the pore geometry often make it difficult to determine the key parameters affecting the behavior, and then predict other situations, particularly as the number of experiments that can be performed in a reasonable time is limited. In particular, the deposition of nanoparticles is important, since this is the mechanism by which, in oil recovery applications for instance, the surface wettability changes, potentially increasing the amount of oil produced [28]. An alternative approach is to use numerical models to predict behavior trends and quantify nanoparticle flow and deposition.

Several approaches have been used to study pore-scale flow and transport of nanoparticles. The Colloid Filtration Theory (CFT) has been extensively employed to examine the retention coefficient of particles under different circumstances and conditions [29]. In CFT, the porous medium is represented by spherical collectors. Then, their contact efficiency is computed in a fluid environment containing nanoparticles immersed in the solution. Using this method, researchers have developed a model to calculate the aggregation of particles of different sizes [30], studied the transfer and retention of nanoparticles in porous media at the pore-scale [31], and calculated the kinetic retention coefficient [32]. However, for realistic results, it is imperative to incorporate actual pore-space geometries in the simulations. In this regard, direct simulation methods that incorporate the pore space in the computational mesh offer broader applicability compared to CFT.

Particle-based simulation, such as the lattice Boltzmann method (LBM) has been widely used to study transport in porous media [33–35]. For example, Zhang et al. [36] modeled solute transport in unconsolidated packed beds. Parvan et al. [37] simulated particle clogging and the resultant impact on permeability. Furthermore, machine learning has been used to predict the results of LBM simulations of colloid transport [38]. The study incorporated models for attachment, detachment, and clogging. Along with the LBM, molecular simulation methods such as molecular dynamics (MD) [39] and Monte Carlo (MC) methods [40,41], have also been used to study transport at the pore scale.

In addition, grid-based and hybrid methods have been used to simulate nanofluid flow: the Eulerian method computes concentration changes in a fixed mesh [42,43], while the Lagrangian method tracks individual particles through space [44–46]. The Eulerian framework has been used extensively to investigate nanofluid heat transfer in porous

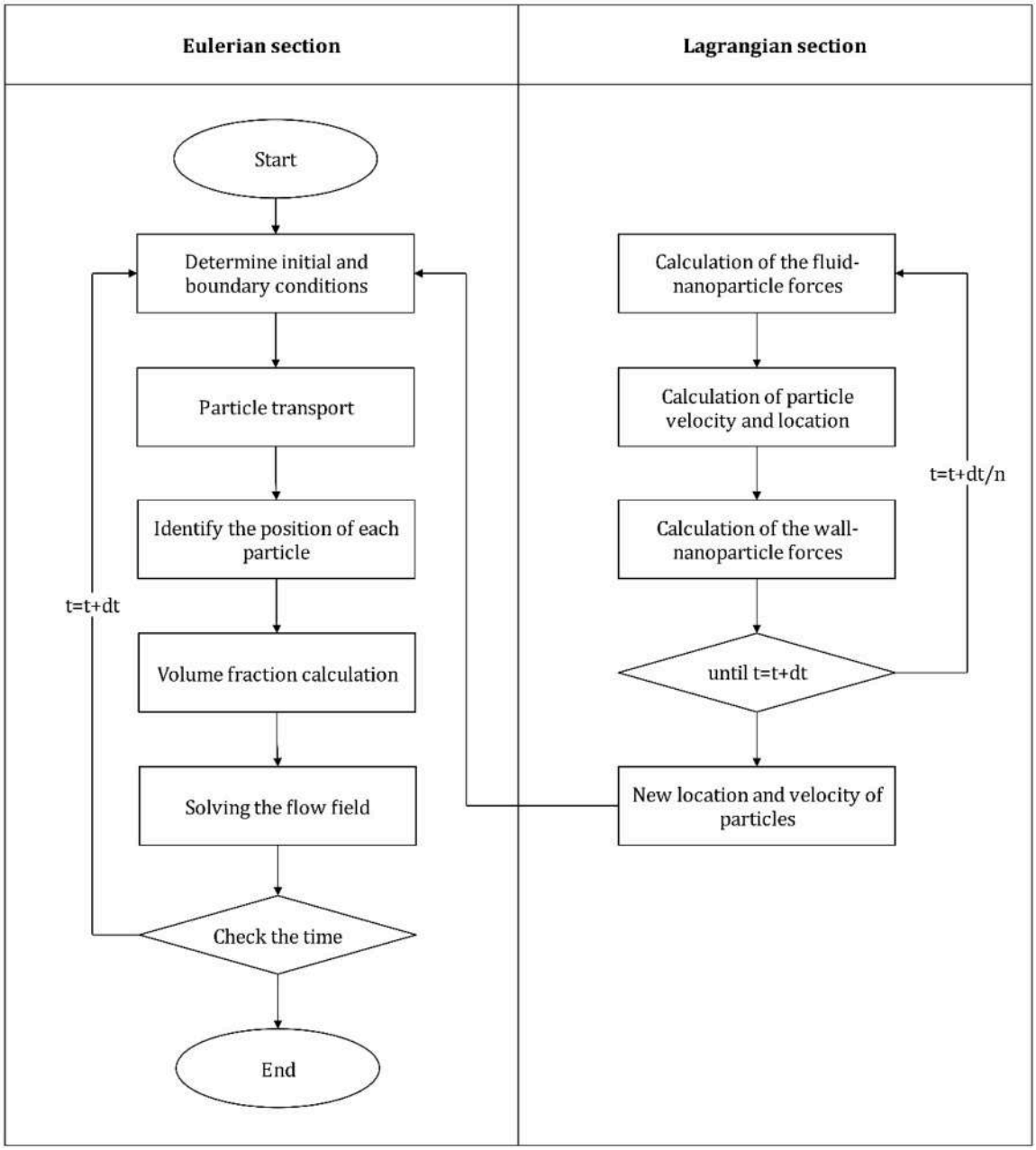

Fig. 1. Solution procedure for the modified solver used in this study.

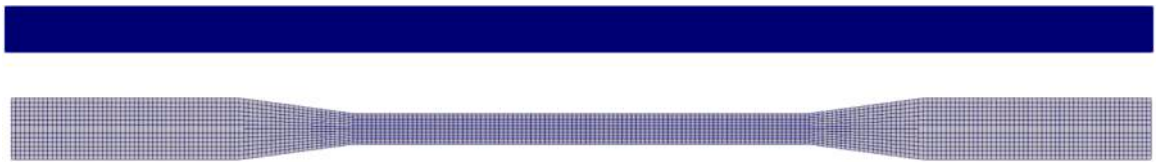

Fig. 2. A schematic representation of two microchannels: (top) the microchannel with 10 μm height and 250 μm length; (bottom) the microchannel with 6.76–13.34 μm height and 250 μm length with a representation of the computational mesh used.

media [47–50]. Despite its limitations, this approach remains a prevalent technique for modeling nanofluid flow within porous media, particularly in the context of heat transfer [51]. Regardless its wide applications, single-phase nanofluid flow simulation cannot predict the complexity of the interaction between nanoparticles and the base fluid. Eulerian two-phase methods show better results in nanofluid flow behavior prediction when compared to single-phase methods. In one of these studies, Seetha et al. [52] modeled nanoparticle transport in a single pore considering Brownian, VDW, and EDL forces in an Eulerian framework. Moreover, a recent work investigated heat transfer and transport of nanofluids in porous media [53]. Buongiorno's model was assumed and an Eulerian approach was used to study the effect of the Brownian motion on the heat transfer.

Although Eulerian methods have their advantages, Lagrangian

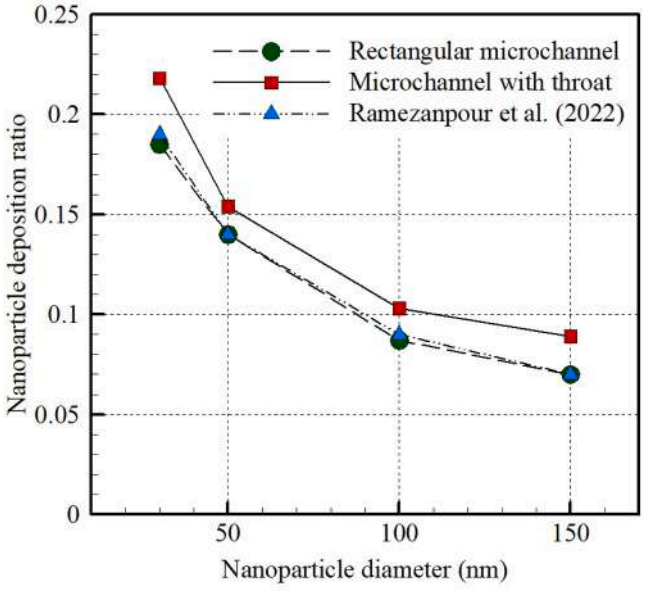

Fig. 3. Nanoparticle deposition ratio as a function of nanoparticle diameter (nm) in two microchannels compared to the results of a previous study [61].

methods can achieve greater accuracy in solving problems because they allow for the tracking of individual particles. Thus, in recent years, the advancement of hardware infrastructure has made the utilization of Lagrangian methods more appropriate. Hence, in simulating flow of nanoparticles and the base fluid, most simulation studies have used a combined Eulerian-Lagrangian (EL) approach: the flow field is solved on a fixed mesh, while nanoparticles are then tracked through the computational domain in a Lagrangian framework [54]. The EL approach was used to investigate the dispersion of nanoparticles in air, for instance [55,56]. Furthermore Andarwa et al. [57,58], used the EL method to study nanoparticle transport and deposition in air in a microchannel. In their simulation, the effect of the dominant forces between nanoparticles and air were considered. However, since air was the base fluid, the effects of parameters related to electrostatic double layer (EDL) force were neglected. Continuing the previous studies in nanofluid flow simulation in a microchannel, Sharaf et al. [59] analyzed the convective heat transfer of nanofluids. Furthermore, developing the EL approach for particle-fluid flow simulation, Sadeghnejad et al. investigated the retention of micro-particles in a packing of glass beads [60]. An overlooked aspect in previous studies on simulating nanofluid flow using the EL method is the omission of forces between the solid surface and particles. To quantify the deposition of particles to the solid walls of a porous medium, electrostatic double layer (EDL) and Van der Waals (VDW) forces need to be considered, as well as the effect of Brownian motion [54].

As mentioned above, there has been significant progress in the simulation of nanofluid flow in porous media. Although Eulerian methods have the advantage of faster solution speeds, they do not allow for particle tracking and the investigation of individual particle behavior. Furthermore, in the studies utilizing Lagrangian methods, certain forces, particularly those between nanoparticles and the wall, have been overlooked, or the impact of different parameters on nanoparticle behavior, particularly in intricate geometries, has not been explored. Hence, developing a computational solver based on the EL method that can model the impact of various forces on nanoparticles is an area that has potential for further exploration. Hence, this study addresses the necessity of developing a computational solver capable of simulating nanofluid flow.

In the present investigation a solver is developed in an open-source library to effectively simulate the dynamics of nanofluid flow within realistic porous media at the micrometer scale. This work builds upon the authors' prior investigation [61], which primarily focused on a straightforward geometric framework. The present study has examined the impact of all effective forces acting on nanoparticles, with particular emphasis on the forces acting between nanoparticles and the solid surface; including the drag, Brownian motion, EDL, and VDW forces. Furthermore, the flow, transport, and attachment of nanoparticles in

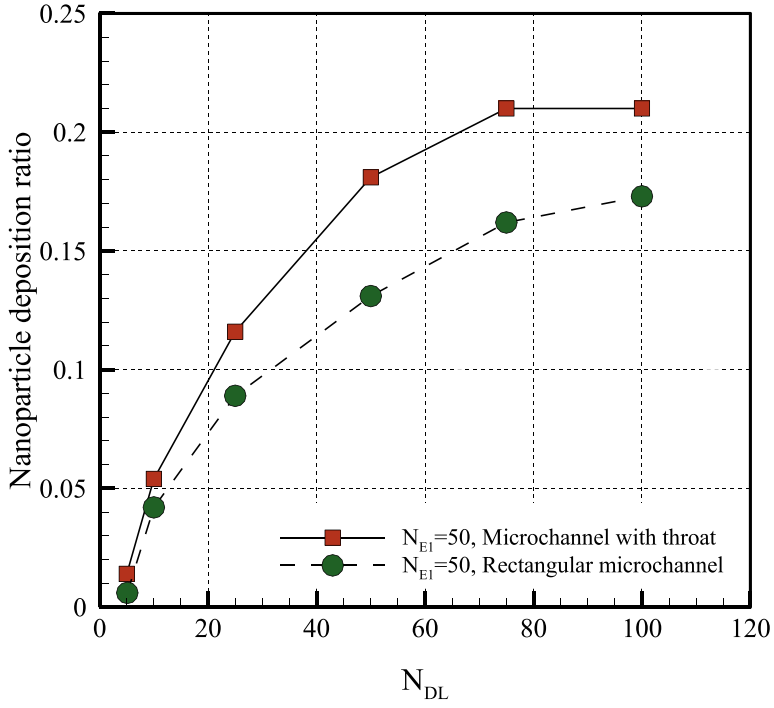

Fig. 4. Nanoparticle deposition ratio as a function of double-layer thickness, N_{DL} in two microchannels.

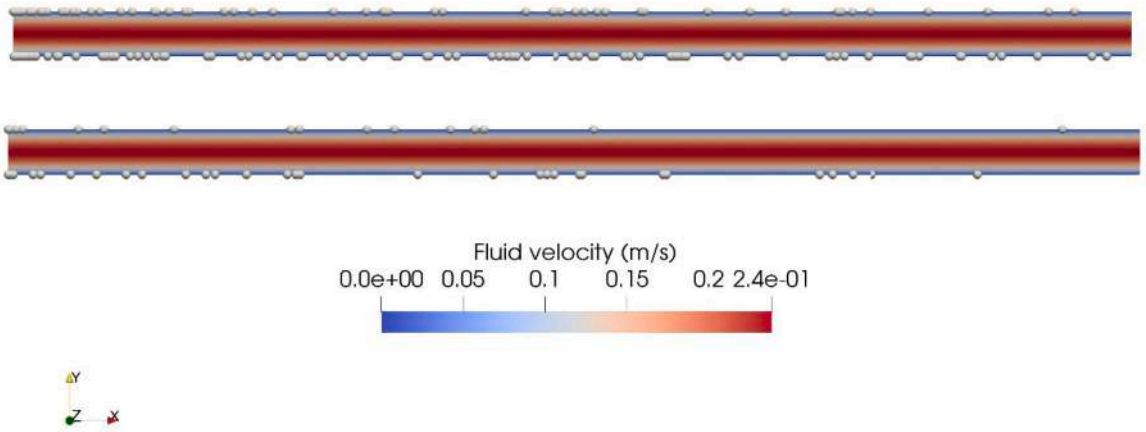

Fig. 5. Deposited nanoparticles on the microchannel surfaces with the rectangular microchannel: top, nanoparticles with diameter d_p=30 nm; and bottom, nanoparticles with diameter d_p =100 nm.

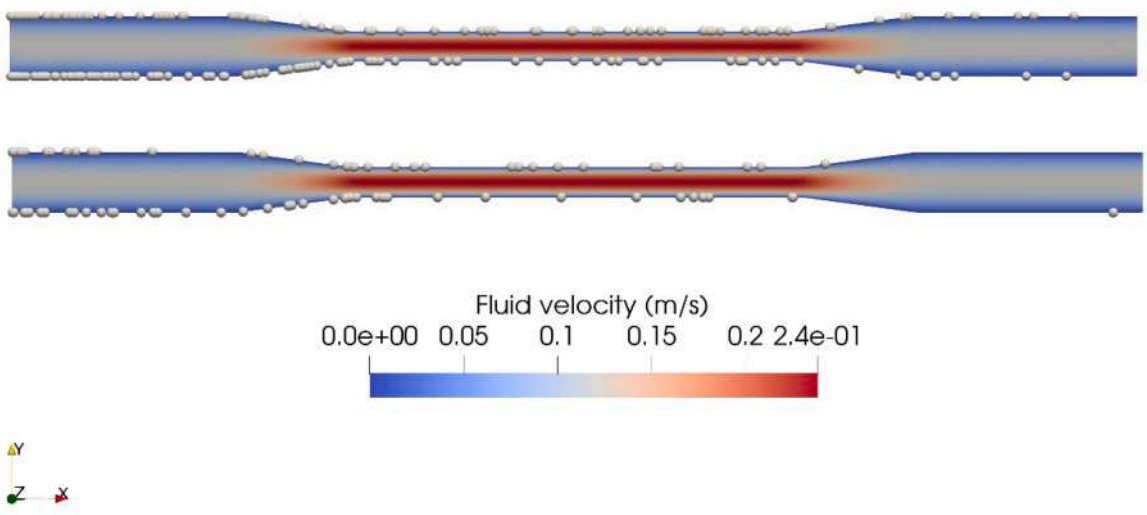

Fig. 6. Deposited nanoparticles on the microchannel surfaces in the microchannel with throat: top, nanoparticles with diameter d_p =30 nm; and bottom, nanoparticles with diameter d_p =100 nm.

complex three-dimensional structures of the Berea sandstone and open-cell foams (OCFs) with different porosities have been simulated. The nanofluid examined in this work was deemed to be dilute, so the interaction and contact between nanoparticles were disregarded. The effect of parameters such as porosity, double-layer thickness, surface potential, and nanoparticle diameter on retention has been investigated.

2. Porous media construction

To accurately simulate the flow of nanofluid in a porous medium, it is crucial to employ appropriate geometries that accurately represent those present in representative applications. A typical instance of one of these geometries is Open-cell foams (OCFs). OCFs are porous structures with low density and high permeability. Ceramic and metallic OCFs enhance the chemical and thermal performance of thermal energy storage units [62,63], heat exchangers [64,65], burners [66], solar collectors [67], and chemical reactors [68]. Various methods can be used to construct model representations of these foams. Weaire–Phelan (WP) and Kelvin unit cells have been widely used to represent the structure [69]. An alternative and more flexible method, Voronoi tessellation (VT) and Laguerre-Voronoi tessellation (LVT) algorithms have been developed to construct the foam with the appropriate quality [70,71], following the approach below [72,73]:

- Spheres are produced with specified sizes.
- Distribute the spheres to fill the internal space of the cube; the sphere radii are not constant, without overlap between the spheres.
- The LVT algorithm is applied.
- The OCF struts are constructed.
- The final geometry is corrected.

In this study, using the LVT approach, three OCFs were constructed using the method of Sepehri and Siavashi [72]. The properties of OCFs used are shown in Table 1.

In addition, to represent a rock sample, a high-resolution X-ray image of Berea sandstone used in the work of Dong and Blunt [74] provides another representation of the pore space. The image porosity is 19.6 %, and the voxel size is 5.345 μm. A $1 \times 1 \times 1$ mm^3 section of the microtomography image was selected for the simulations.

3. Theoretical background

Nanofluid flow was solved using the Eulerian-Lagrangian method, as discussed in the preceding sections. It is assumed that the flow is incompressible and the temperature is constant. The governing equations are as follows for steady-state flow (see [75]). The first is conservation of mass:

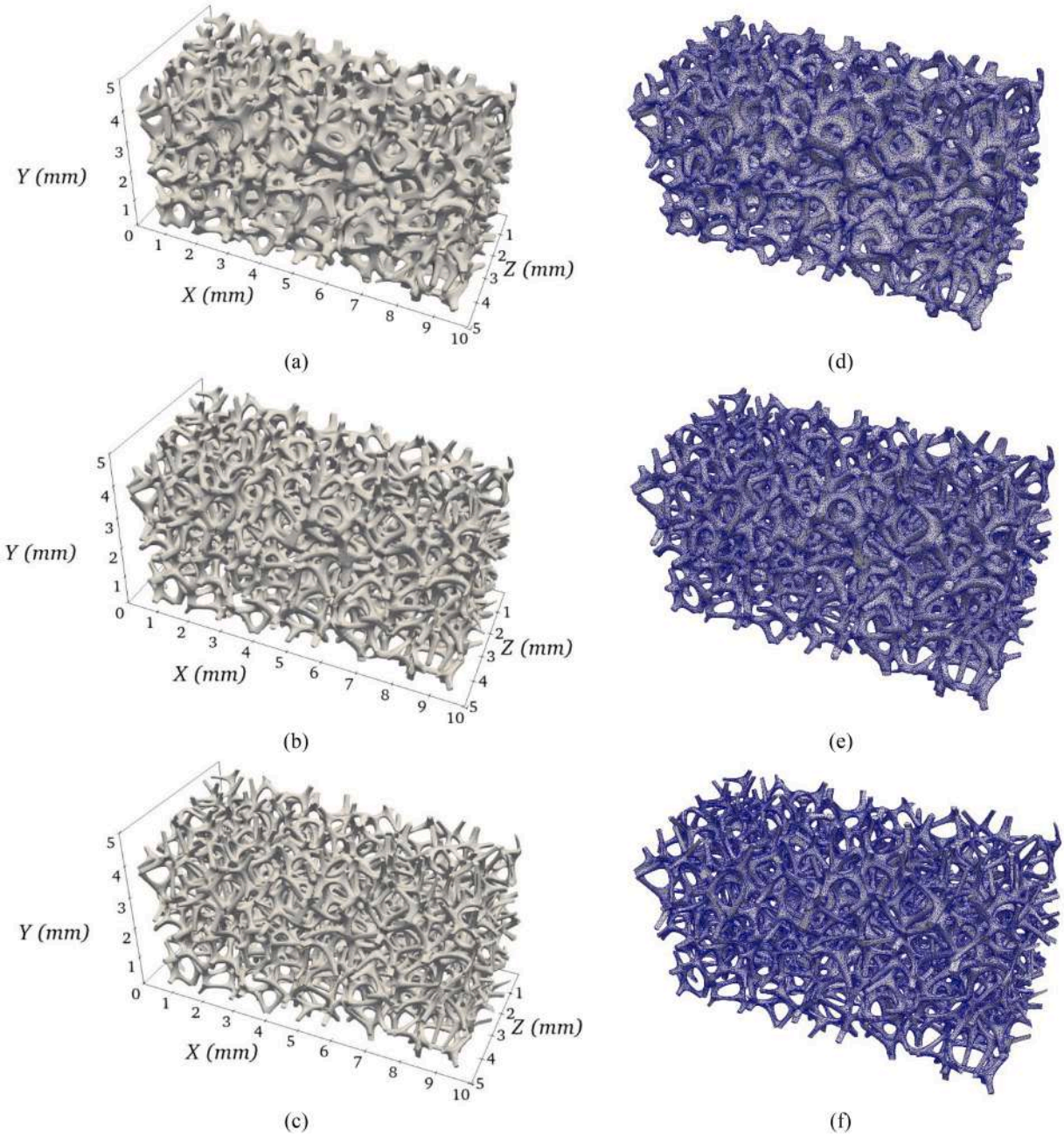

Fig. 7. Three samples of OCFs: left (a, b, and c), geometries of samples 1, 2, and 3 from top to bottom with 80 %, 85 %, and 90 % porosity; and right (d, e, and f), the mesh created for each sample.

$$\nabla.(\rho_f U_f) = 0 \tag{1}$$

where the U_f, and ρ_f are the velocity and density of the fluid, respectively.

The second equation applies conservation of momentum using the steady-state Navier-Stokes equation:

$$\rho_f(\boldsymbol{U}_f.\nabla)\boldsymbol{U}_f = -\nabla p + \nabla.\left[\mu_f\left(\nabla \boldsymbol{U}_f + \nabla \boldsymbol{U}_f{}^T\right)\right] + S_m \tag{2}$$

where S_m is the source term (momentum transfer between the nanoparticles and fluid) computed as follows [54]:

$$S_m = \frac{1}{\delta V}\sum_{p=1}^{n_p} m_p \boldsymbol{F}_p \tag{3}$$

where m_p is the mass of the particle.

The EL approach calculates the force between nanoparticles and the fluid. The concentration of nanoparticles is such that the solution is considered dilute. Hence, particle-particle collisions and interactions are neglected. Also, due to the negligible effect of nanoparticle transport on fluid flow, the one-way coupling method is utilized. Consequently, to compute the force exerted on nanoparticles by the Lagrangian approach, Newton's second law is used as follows [54]:

$$m_p \frac{d\boldsymbol{U}_p}{dt} = \boldsymbol{F}_p \tag{4}$$

$\boldsymbol{F}_p$ indicates all forces exerted on an individual particle in the nanofluid flow. This force includes nanoparticle-fluid and nanoparticle-wall forces.

We reviewed previous work to determine the principal forces

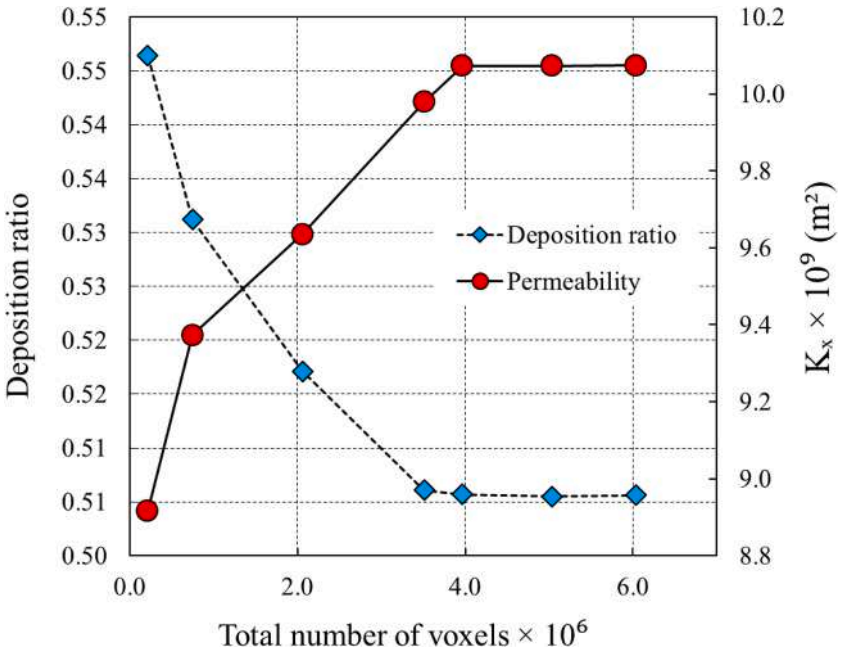

Fig. 8. Mesh dependence of nanoparticle deposition and permeability for different numbers of simulation voxels.

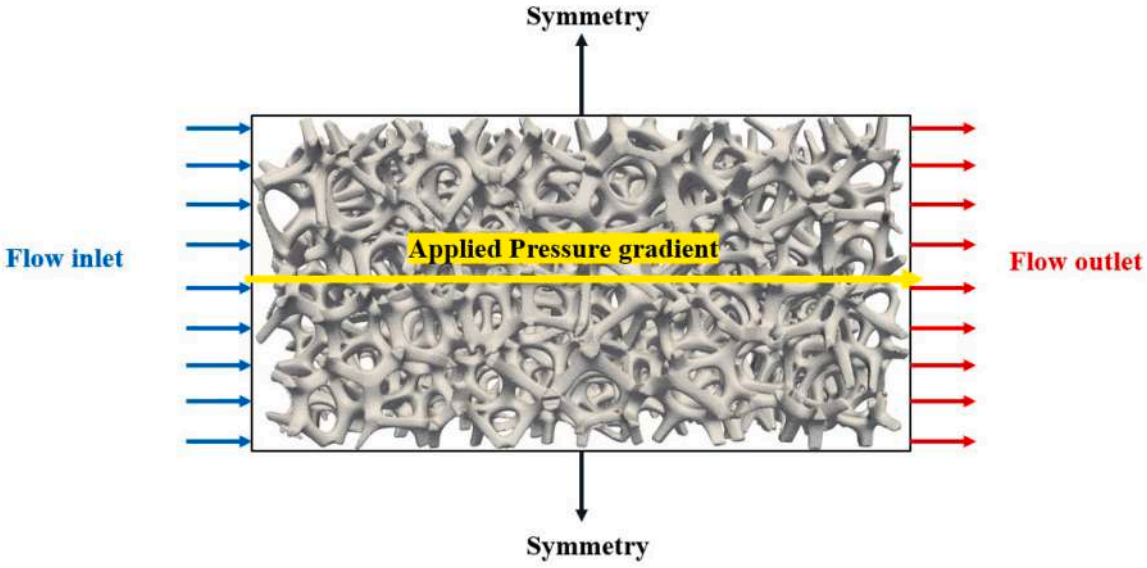

Fig. 9. The initial and boundary conditions in a two-dimensional schematic picture of an OCF.

affecting nanoparticle flow. Marshall and Li [76] provided a scaling study for micrometer-scale particle flows, while Buongiorno [77] and Savithiri et al. [78] provided scaling analyses for nanofluids. Based on this work we can reach the following conclusions [54]:

1. Fluid drag remains the most significant factor, however, the inertia reduces fast as the particle size decreases.
2. Lift forces are insignificant for nanoparticles of small diameter, but becomes more important as the nanoparticle radius increases.
3. The Brownian motion force and thermophoretic effects in nanofluid are comparable to the drag force.

Hence, we consider drag, buoyancy and gravity, Saffman lift, and Brownian motion [52,57–59]. Also, EDL and VDW are the main forces between the nanoparticles and the solid. Hence Eq. (4) is rewritten as follows [54,57]:

$$m_p \frac{d\boldsymbol{U}_p}{dt} = \boldsymbol{F}_{Br} + \boldsymbol{F}_D + \boldsymbol{F}_{SL} + \boldsymbol{F}_G + \boldsymbol{F}_B + \boldsymbol{F}_W \tag{5}$$

Brownian motion, the random movement of particles and their collisions, is dominant in nanofluid flow. It is modeled as Gaussian white noise [79]:

$$\boldsymbol{F}_{Br,i} = m_p \varsigma_i \sqrt{\frac{216 \mu_f k_b T}{\pi \rho_p{}^2 d_p{}^5 C_c \Delta t}} \tag{6}$$

where, i shows the direction of Brownian motion force, T is the temperature, d_p is the nanoparticle diameter, k_b is the Boltzmann constant (equals $1.3806 \times 10^{-23} \mathrm{m^2 kg/(s^2 K)}$), and Δt is the time-step. This force is calculated at each time step. At first, a time step is chosen, and a sequence of random numbers (between 0 and 1) are generated. In the following, the pairs of random numbers are transformed into pairs of

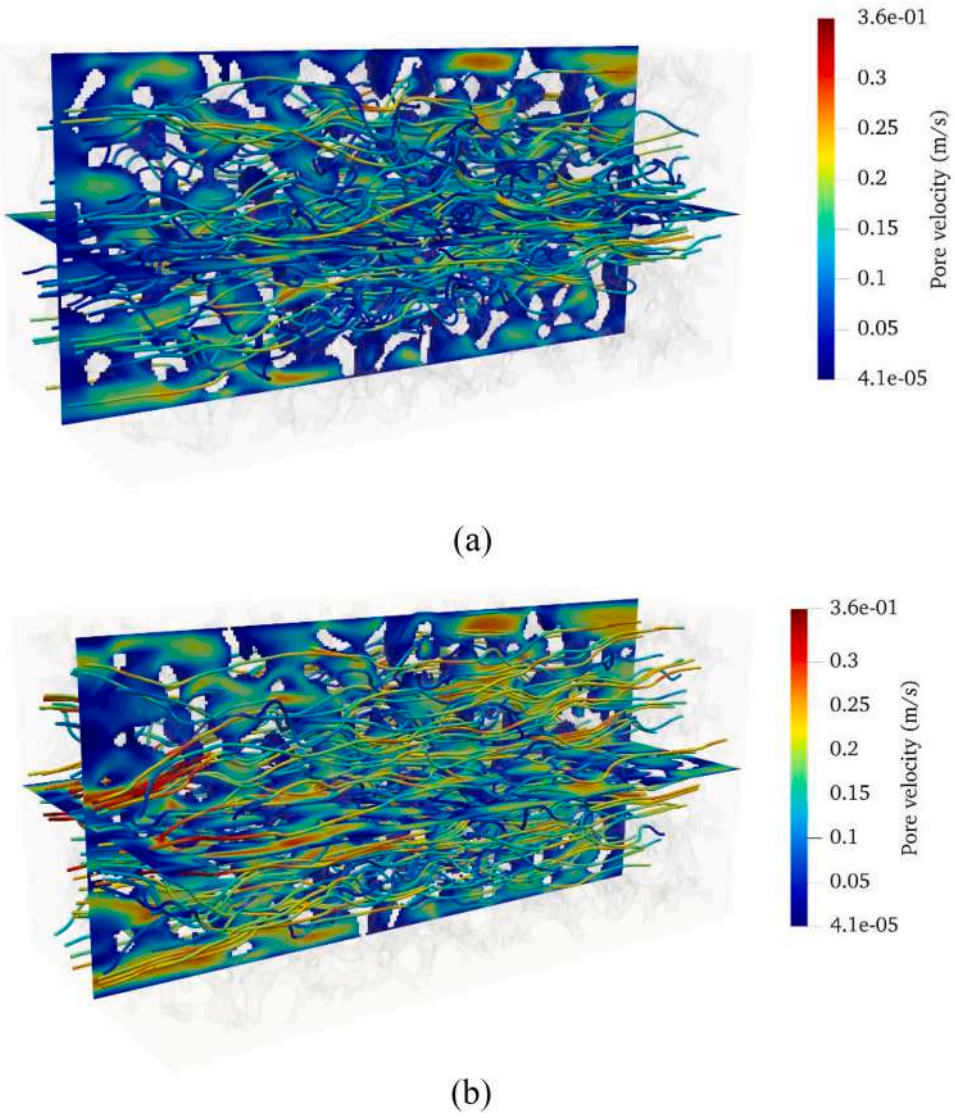

Fig. 10. Magnitude contours of the pore velocity for (a) sample 1: PPI30, porosity =80 % and (b) sample 2: PPI30, porosity =85 %.

zero-mean Gaussian random numbers with unit variances by $\varsigma_1 = \sqrt{-2\ln(A_1)}\cos(2\pi A_2)$ and $\varsigma_2 = \sqrt{-2\ln(A_1)}\sin(2\pi A_2)$. In this equation, A_1 and A_2 are random numbers between 0 and 1. Additional details of this approach are provided in [80]. These values are put in Eq. (6) to calculate the Brownian motion force.

Drag is another decisive force in nanofluid flow problems. This force is exerted against the particle movement due to the relative motion of the particle with respect to the fluid [57]:

$$\boldsymbol{F}_{Drag} = m\frac{18\mu_f}{\rho_p {d_p}^2 C_c}(\boldsymbol{U} - \boldsymbol{U}_p) \tag{7}$$

The Cunningham slip correction factor (C_c) has been developed empirically [81]. Since the no-slip condition is not valid for nanoparticles, this parameter is used to modify the drag force. C_c is calculated as follows [81]:

$$C_c = 1 + \mathrm{Kn}\left(\alpha + \beta\exp\left(-\frac{\gamma}{Kn}\right)\right) \tag{8}$$

where α, β, and γ are 1.165, 0.483, and 0.997, respectively. Also, the Knudsen number (Kn) is defined as the ratio of the mean free path of fluid molecules (λ) compared to the particle radius (r_p), $\mathrm{Kn} = \lambda/r_p$.

Drag and Brownian motion forces, which are in the same order of magnitude, are the main forces between the fluid and nanoparticles [54].

Saffman lift is a force that is perpendicular to the direction of particles in a shear flow, which is calculated as follows [82]:

$$\boldsymbol{F}_{\mathrm{Saffmann}} = 6.46{r_p}^2(\boldsymbol{U} - \boldsymbol{U}_p)\sqrt{\rho\mu\left|\left(\frac{\partial \boldsymbol{U}}{\partial y}\right)\right|}\,\mathrm{Sign}\left(\frac{\partial \boldsymbol{U}}{\partial y}\right)\boldsymbol{e}_y \tag{9}$$

The sum of buoyancy and gravity forces is represented as [54]:

$$\boldsymbol{F}_{Bouyancy} + \boldsymbol{F}_{Gravity} = \left(\pi\frac{{d_p}^3}{6}\right)(\rho_f - \rho_p)\boldsymbol{g} \tag{10}$$

Nanoparticle deposition on solid surfaces depends on the forces between the particles and the wall, which is very large close to the solid (nanometer scale). The DLVO theory was developed as a computational model to study the stability of colloidal dispersions [83]. EDL and VDW forces were considered in the DLVO theory. Hence, $\boldsymbol{F}_W$ in Eq. (5) can be written as follows:

$$\boldsymbol{F}_W = \boldsymbol{F}_{VDW} + \boldsymbol{F}_{EDL} \tag{11}$$

The VDW force is attractive between solid surfaces and nanoparticles. This force is noticeable at distances of several 10 s nm [84]. The VDW force between a particle and a surface is calculated as follows

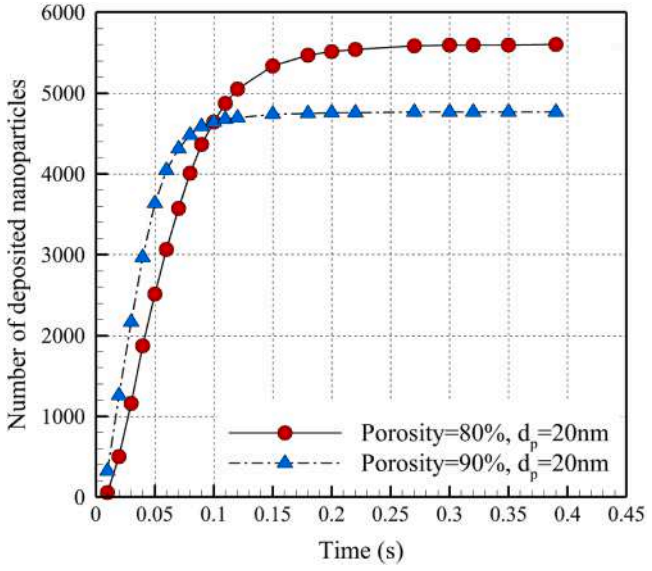

Fig. 11. Number of deposited nanoparticles with 20 nm diameter as a function of time (s).

[85]:

$$\boldsymbol{F}_{VDW} = \frac{A_H}{6}\left[-\frac{r_p}{(z-r_p)^2} - \frac{r_p}{(z+r_p)^2} + \frac{1}{z-r_p} - \frac{1}{z+r_p}\right] \tag{12}$$

where A_H is the Hammaker constant for a spherical nanoparticle.

Moreover, the EDL force is also significant at nano-scale distances in liquids with a high dielectric constant; an EDL forms around the ionized particles [86]. The EDL force between various surfaces is calculated using the Hogg-Healy-Fuerstenau (HHF) formulae as follows [86]:

$$\boldsymbol{F}_{EDL} = 2\kappa\pi\varepsilon\varepsilon_0 r_p\left(\psi_1{}^2 + \psi_2{}^2\right)\left[\frac{\frac{2\psi_1\psi_2}{\psi_1{}^2+\psi_2{}^2} - \exp(-\kappa z)}{\exp(\kappa z) - \exp(-\kappa z)}\right] \tag{13}$$

where κ is the inverse of the Debye-Huckel length, ε is the dielectric constant of the solution, ε_0 is the permittivity of a vacuum, and ψ_1, and ψ_2 are the surface potential of particles and solid surfaces. In calculating the EDL force, three dimensionless parameters are introduced [87]:

$$\mathrm{N_{E1}} = \frac{\pi\varepsilon\varepsilon_0 \mathrm{r_p}(\psi_1{}^2 + \psi_2{}^2)}{\mathrm{k_B T}} \tag{14}$$

$$\mathrm{N_{E2}} = \frac{2\psi_1\psi_2}{\psi_1{}^2 + \psi_2{}^2} \tag{15}$$

$$\mathrm{N_{DL}} = \kappa r_p \tag{16}$$

where N_{E1} and N_{E2}, show the magnitude and ratio of surface potentials, respectively and N_{DL} represents the ratio of particle radius to double layer thickness.

Using Eqs. (14)-(16), Eq. (13) is rewritten as follows:

$$\boldsymbol{F}_{EDL} = 2\kappa k_B T N_{E1}\left[\frac{N_{E2} - exp(-N_{DL}z^*)}{\exp(N_{DL}z^*) - \exp(-N_{DL}z^*)}\right] \tag{17}$$

where $z^* = \frac{z}{r_p}$. The physical characteristics of nanoparticles and fluids are presented in Table 2. The primary focus of this study was on iron nanoparticles.

3.1. Solver development

The EL solver is based on the open-source library of the OpenFOAM. The details of the solver specifications are provided in the previous study by Ramezanpour et al. [61]. Using the finite volume method (FVM), the

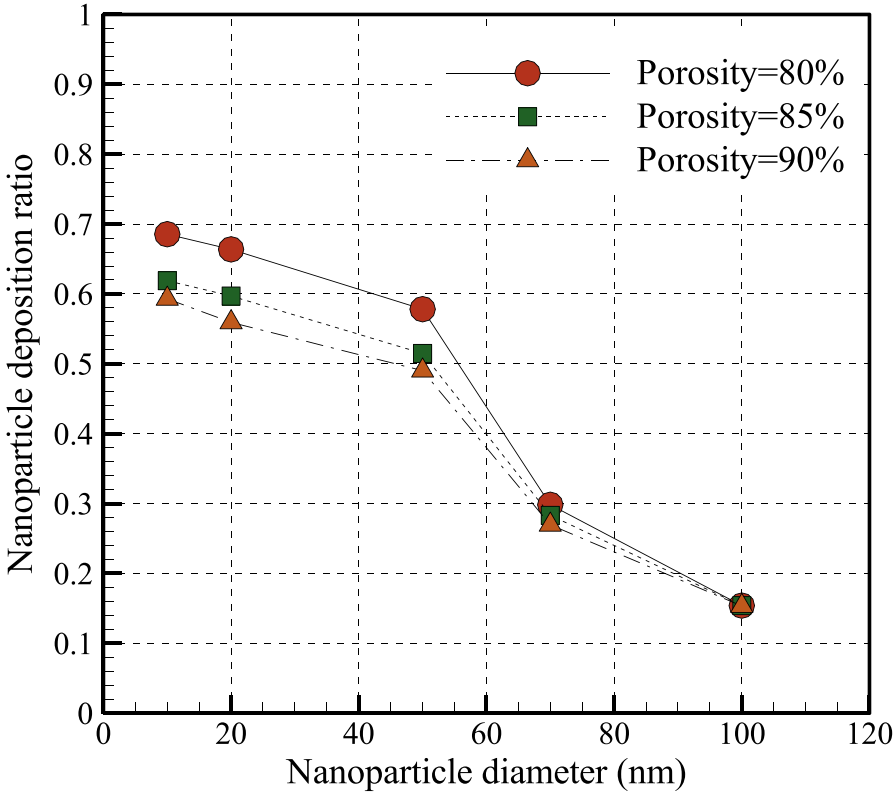

Fig. 12. Nanoparticle deposition ratio as a function of nanoparticle diameter for different samples with porosities of 80, 85, and 90 percent.

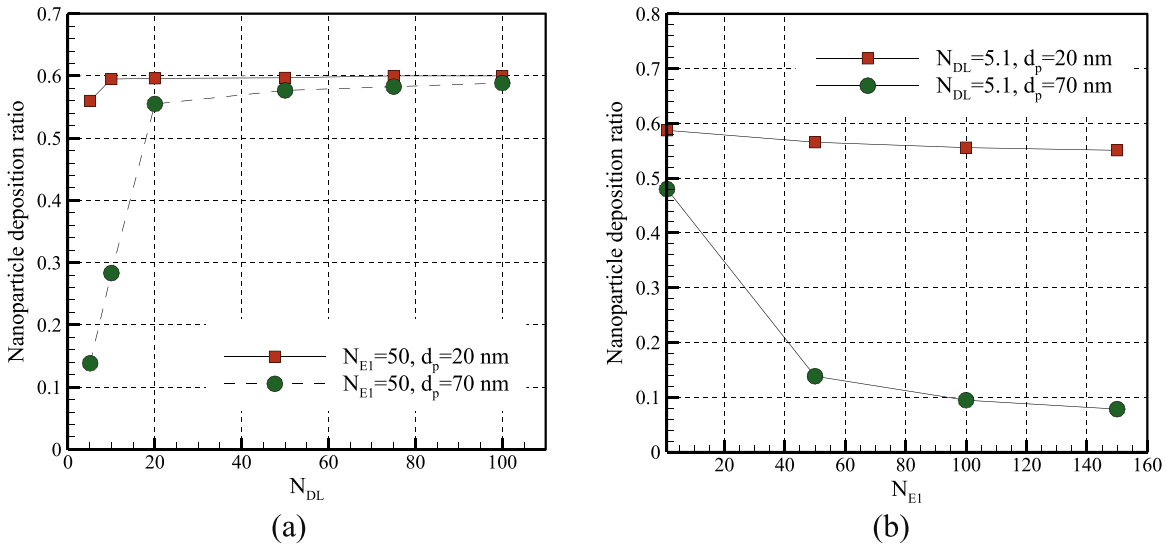

Fig. 13. The deposition ratio of nanoparticles with 20 and 70 nm diameters in OCF with 85 % porosity as a function of (a), N_{DL}, and (b), N_{E1}.

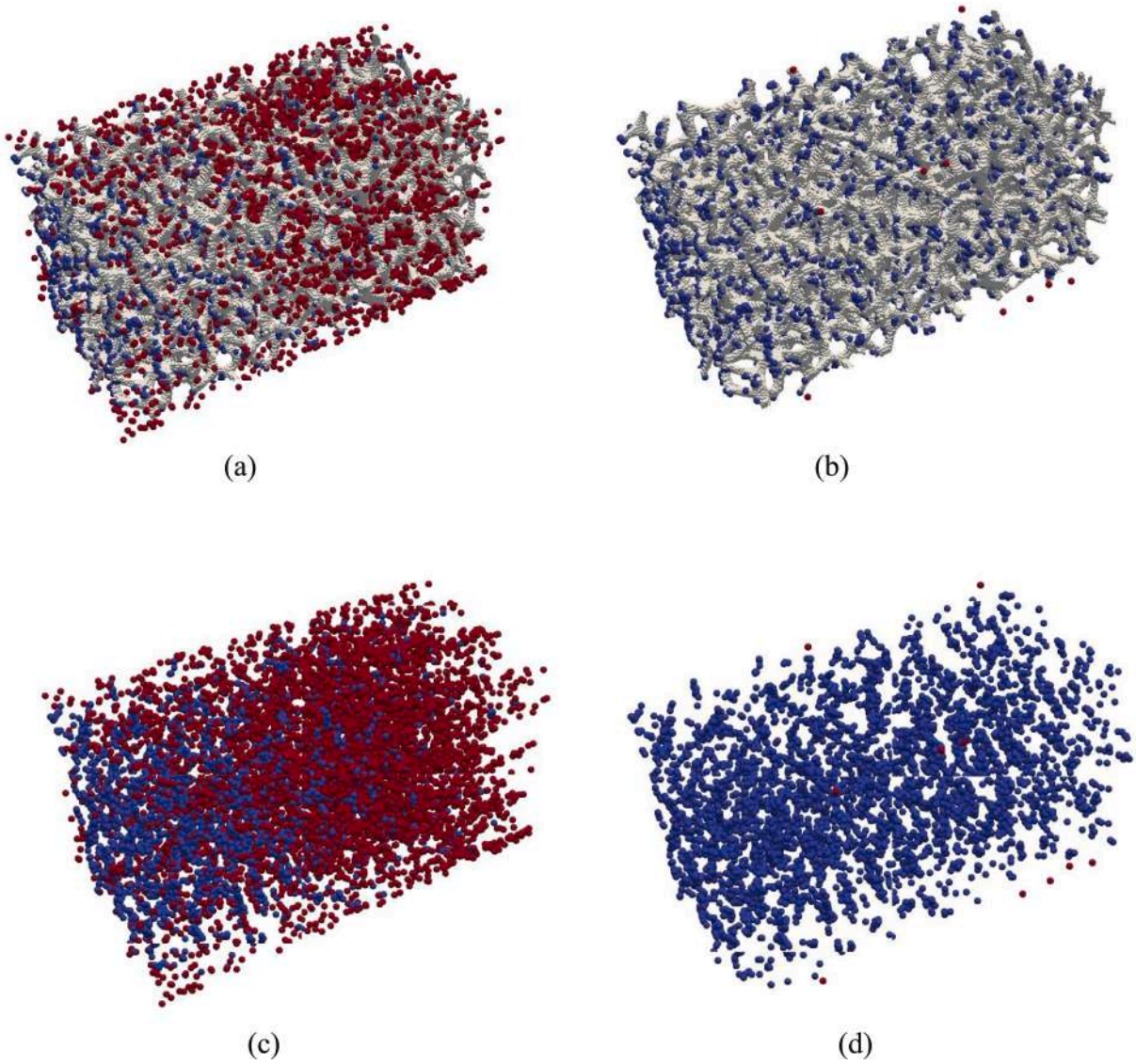

Fig. 14. The deposited and moving nanoparticles in OCF-2 (with 85 % porosity) are shown in blue and red, respectively. Left (a, c), $t = 0.05$ s, and right (c, d), $t = 0.4$ s. The bottom pictures show the nanoparticles without the solid.

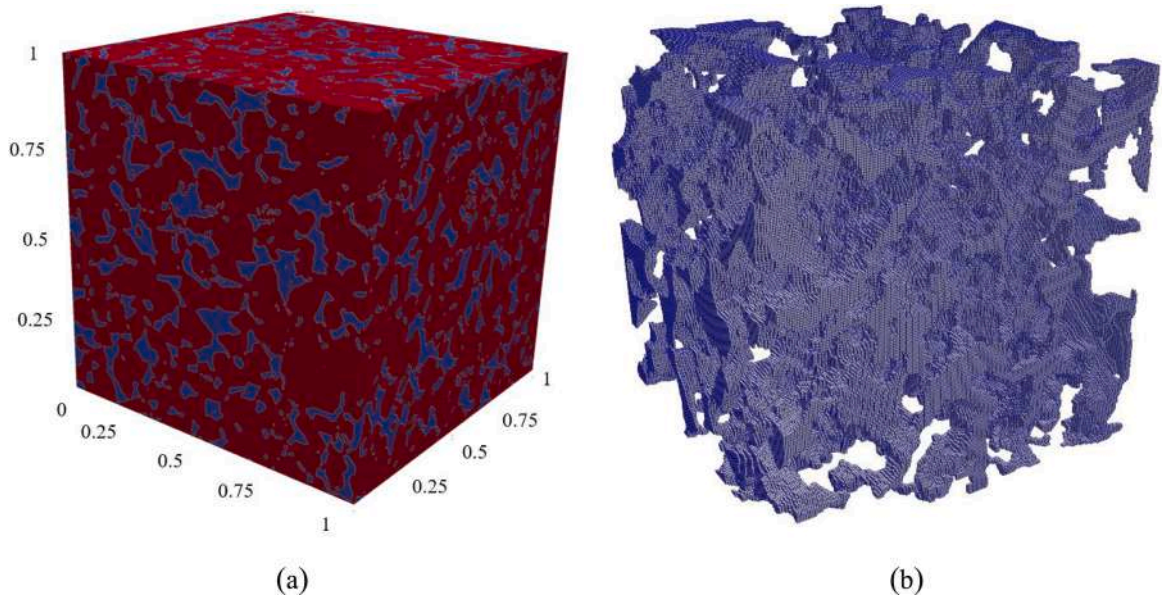

Fig. 15. The geometry of Berea sandstone (a) accompanied by mesh created (b).

Lagrangian solver is paired with the PIMPLE algorithm (a combination of PISO and SIMPLE algorithms).

The particle locations and velocities are obtained from the Lagrangian solver and are then transmitted to the Eulerian part of the code. Calculating the particle volume fraction inside each cell is the next procedure. The fluid forces (drag, lift, etc.) acting on each particle are computed using the particle and fluid initial velocities as well as the particle volume fraction by the use of Eqs. (5)-(17). Then momentum exchange terms between particles and fluids are computed by Eq. (3). The updated velocity and position of the nanoparticles are determined in the following step. The flow field and the fluid pressure and velocity are calculated in the Eulerian section using Eqs. (1)-(3). The solution process is depicted in Fig. 1. A central difference scheme with second-order accuracy is used to discretize the pressure gradient. The first-order Euler scheme discretized time derivatives [88]. Algebraic and geometric multi-grid preconditioning for pressure and the Gauss-Seidel smoothing for velocity are used to solve the results of the Eulerian discretized system by a conjugate gradient solver.

The solver settings are such that deposition of nanoparticles occurs when the attractive forces with the solid surfaces of the porous medium are greater than repulsion: when the distance from the center of the nanoparticle to the nearest solid surface is less than the radius of the nanoparticle, the nanoparticle is deposited [57,89]. Moreover, the following assumptions are made in all problems of this study.

- Nanoparticles are injected over a short time (about 10^{-7} s) at the beginning of the simulation process.
- The entry velocity of the particles is 80 % of the fluid velocity [57].
- The distribution of nanoparticles in the inlet of the porous media is random.
- The simulation of nanoparticle migration continues until the last particle deposits or escapes.
- Drag, Saffman lift, Brownian, buoyancy, gravity, VDW, and EDL are the forces that affect nanoparticles.

The simulations were executed parallel on a workstation equipped with 2 Intel® Xeon® CPUs, each consisting of 16 threads operating at a frequency of 3.3 GHz, and 64 GB of computational memory.

4. Results and discussion

In this section, the simulation of nanoparticle flow in various geometries is conducted using the solver function developed in the previous section, based on the governing equations of the Eulerian-Lagrangian method. The results of these simulations are then presented. The results will be presented in three sections: 1) microchannel with different cross sections, 2) three OCFs, and 3) Berea sandstone. In all three sections, the water is the base fluid.

We build upon our previous study [61] to investigate the accuracy of the computational solver while examining the dynamics of nanoparticle flow in complex porous medium geometries. Furthermore, the impact of different forces and particle size on the flow characteristics of nanoparticles will also be examined.

4.1. Nanoparticle deposition in microchannels

This section investigates nanoparticle transport and attachment in two microchannels with different geometric characteristics. The first microchannel has a length of 250 μm and a height of 10 μm. The length of the second microchannel is 250 μm, the same as the first one, but its height variates from 13.34 μm to 6.76 μm (similar to two pores connected by a narrower throat). However, both microchannels have the same surface area. A schematic representation of these microchannels is shown in Fig. 2.

The ratio of deposited nanoparticles to injected nanoparticles is defined as the nanoparticle deposition ratio [61]. This parameter is calculated for the nanoparticles with different diameters in Fig. 3, with N_{E1} and N_{E2} equal to 1 and N_{DL} being 25. The number of injected particles is 1000. This number is chosen for computational efficiency and to ensure that the solution remains dilute in that the particles do not interact with each other. It is shown that the deposition ratio decreases by approximately 60 % with an increase in nanoparticle diameter from 30 nm to 150 nm, as a result of a 55-fold reduction in Brownian motion, Eq. (6).

In addition, the deposition ratio in the microchannel with a throat is approximately 20 % more than the rectangular microchannel, since the restriction provides a greater surface area to volume ratio. The results for the rectangular channel are almost identical to previous work by Ramezanpour et al. [61].

Furthermore, the influence of the ratio of the particle radius to the

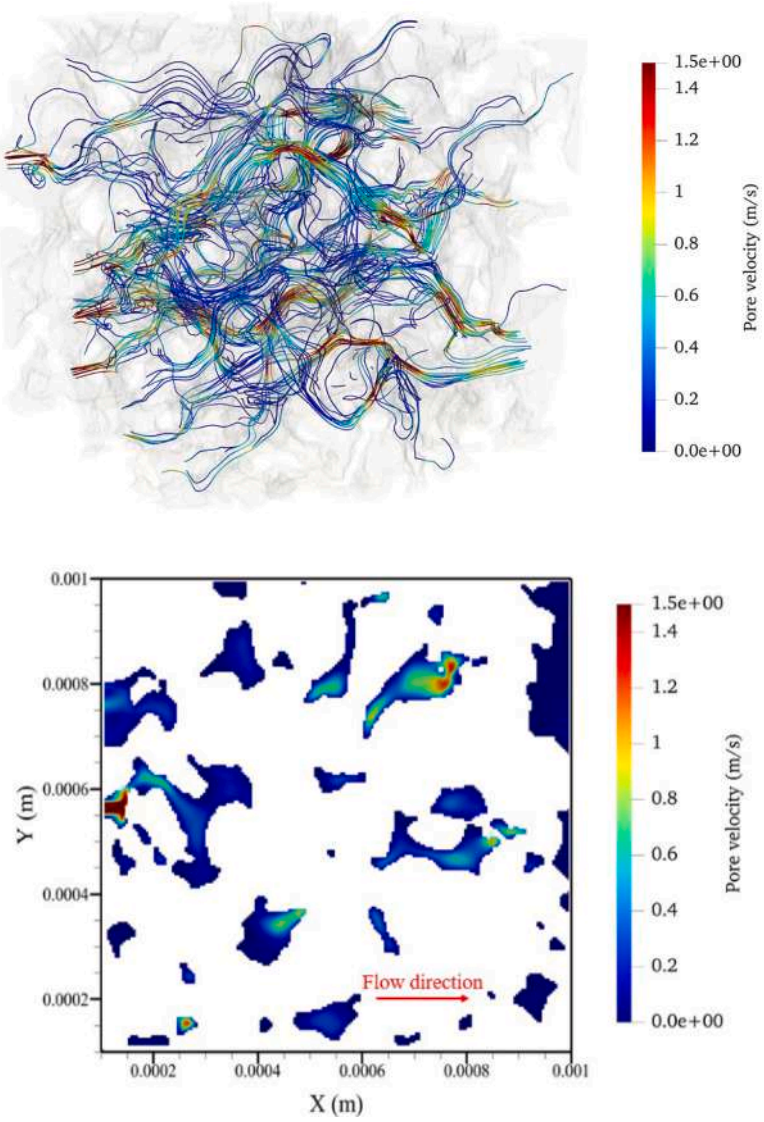

Fig. 16. The sandstone's velocity contours and streamlines in three dimensions and two two-dimensional cross-sections

thickness of the double layer, $N_{DL,}$ on the deposition ratio for the two microchannels is shown in Fig. 4. It has been assumed that N_{E1} is 50 and the particle diameter is 30 nm. With an increase in N_{DL}, the double layer around two surfaces will be compacted for a constant nanoparticle radius. Hence, EDL's repulsive force decreases, enhancing nanoparticle retention. This fact is shown in this figure that agrees with previous studies in the literature [52]. As in Fig. 3, the deposition ratio in the microchannel with a throat is higher than in the rectangular microchannel.

Deposition with 30 and 100 nm diameter particles in the two microchannels is depicted in Fig. 5 and Fig. 6. For better visualization, the dimensions of the nanoparticles are magnified. At $t = 0.04$ s, all the nanoparticles injected in the microchannel have deposited or escaped. The number of deposited nanoparticles with a diameter of 30 nm is 111 % greater than those with a diameter of 100 nm in the rectangular microchannel. This increase in the deposition ratio with a decrease in nanoparticle diameter is also apparent in the microchannel with a throat.

4.2. Nanoparticle deposition in OCFs

The previous section demonstrated that the deposition ratio of nanoparticles in a microchannel with a throat is greater than that in a rectangular microchannel, despite both microchannels having the same area. This outcome suggests that the intricacy of the geometry will directly impact the enhancement of nanoparticle deposition. Nevertheless, the geometry examined in the preceding section is simpler in comparison to porous media characterized by an intricate geometric configuration. Hence in this section, the transport and attachment of nanoparticles in three OCFs were studied. The structure of the OCF samples with the mesh created on them is shown in Fig. 7. The OCF samples have a constant pore density equal to 30 PPI with various porosities (80, 85, and 90 %). The physical properties of the samples are listed in Table 1.

The meshes were generated using the snappy HexMesh (SHM) tool (a mesh generation method in OpenFOAM). To determine the sensitivity to grid resolution, simulations were run with seven mesh resolutions (number of voxels). Fig. 8 shows the results in terms of deposition ratio and permeability: once we have 3.5–4 million voxels, the results appear to be independent of resolution. As a result, this value is considered for the number of voxels in the mesh.

The initial and boundary conditions are depicted in a schematically two-dimensional picture of an OCF in Fig. 9. A pressure gradient is imposed along the input-output boundary to prevent instability in the solutions. The input thermal boundary at the inlet is set to a constant temperature; also, there are no-slip conditions for velocity along the

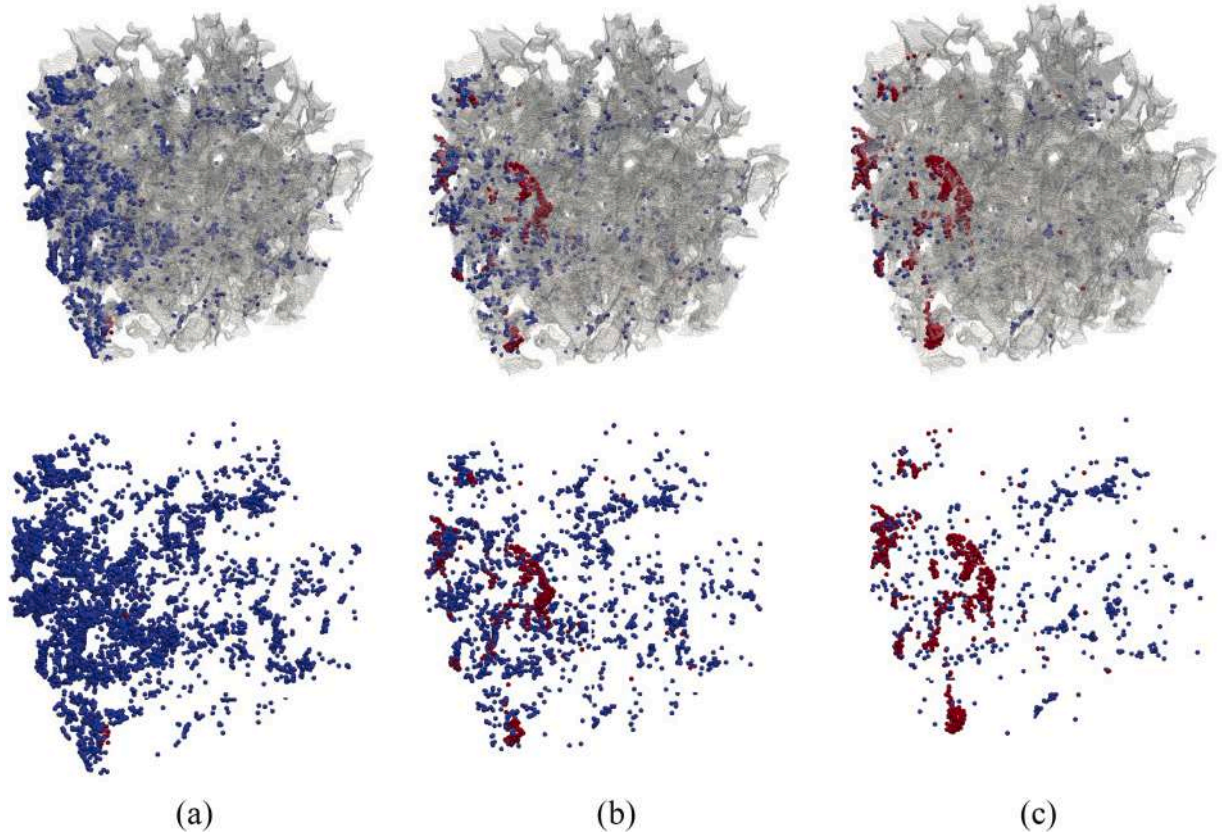

Fig. 17. The deposited and moving nanoparticles in Berea sandstone are shown in blue and red, respectively, and – for the top row – the rock in gray. (a) $d_p = 20nm$, (b) $d_p = 50nm$, and (c) $d_p = 70nm$. The bottom pictures show the deposition of nanoparticles without the solid.

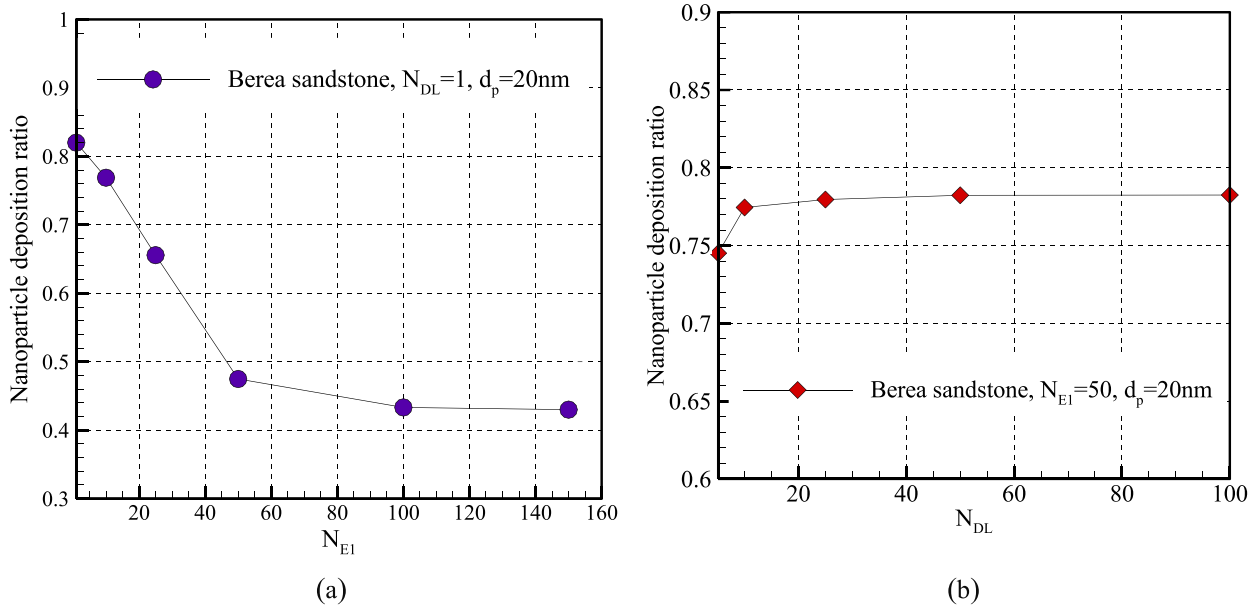

Fig. 18. Nanoparticle deposition ratio in Berea sandstone for d_p=20 nm and different values of (a) N_{E1} and (b) N_{DL}.

surrounding walls.

In this study, the one-way coupling method is used. Hence, we first solve for single-phase flow. Then, the nanoparticle trajectory is calculated by the Lagrangian approach in the fluid flow field. The convergence of each simulation is dependent on the pressure gradients and the number of computational cells, typically necessitating a duration of 12–15 h. For convergence, the time step was selected to be smaller than the particle relaxation time ($\tau_m = \frac{\rho_p D_p^2 C_c}{18\mu_F}$), as reported in references [57, 59]. Distinct time steps were taken into account based on the various solution conditions. However, the values primarily ranged within the order of $10^{-9} - 10^{-10}s$.

Fig. 10 demonstrates the effect of porosity on the velocity contours

and streamlines for samples 1 and 2, for constant pore density. The findings show that the flow patterns in the low porosity voids are more tortuous than the high porosity sample's projected flow patterns. The OCF offers additional flow space in the sample with high porosity, resulting in higher velocities.

The solution process in this problem continues until the last particle deposits or escapes through the system. In Fig. 11, the retention of nanoparticles is evaluated and compared at different times for samples 1 and 3. Ten thousand nanoparticles are injected into the porous media: again this number is chosen for computational efficiency and to ensure that the particles remain in a dilute regime. As is evident in this figure, for the geometry with 80 % porosity, more nanoparticles deposit than the foam with 90 % porosity. It is also found that, for the sample with 80 % porosity, after about 0.27 s, only a few particles (less than 2 %) deposit. This time is about 0.15 s for sample 3 with 90 % porosity. The velocity of nanofluid flow in OCF with 90 % porosity is higher than 80 % porosity. Hence the velocity of nanoparticle migration is higher, and the ultimate deposition ratio occurs in a shorter time. Furthermore, it should be noted that for $t < 0.1$ s, the deposition ratio in OCF with 90 % porosity, occurs in a wider range of geometry. Hence the deposition ratio is slightly more than that of the OCF with 80 % porosity since initially the faster flow allows the nanoparticles to encounter more of the pore space.

The deposition ratio for the three OCF samples is calculated as a function of nanoparticle diameter in Fig. 12. It has been assumed that N_{E1}=50, N_{DL}=10, and N_{E2}=1. The OCF with 80 % porosity has the highest deposition ratio since it has a larger surface area. The deposition ratio of 20 nm diameter nanoparticles in OCF with 80 % porosity is almost 0.1 greater than in OCF with 90 % porosity. This difference decreases to 0.03 for nanoparticles with a 70 nm diameter; it becomes close to zero for a diameter of 100 nm. Hence, in OCFs with high porosity, the effect of porosity on the retention of nanoparticles with a diameter of less than 70 nm is significant but can be neglected for larger nanoparticles.

The deposition ratio of nanoparticles with 20 and 70 nm diameters as a function of N_{E1} and N_{DL} is investigated in Fig. 13. As stated in the explanation of Fig. 4, for a constant nanoparticle radius, increasing N_{DL} has a direct effect on retention. The deposition ratio increases from 0.56 to 0.6 when N_{DL} is increased from 5.1 to 10 with constant values of N_{E1}=50 and d_p=20 nm. However, a further increase in this parameter does not have a noticeable effect. This is also seen for nanoparticles with a diameter of 70 nm when N_{DL} reaches to 50.

With an increase of N_{E1} the surface potential increases such that the repulsion between nanoparticles and the solid becomes larger. Consequently, the attachment of nanoparticles decreases. For N_{DL}=5.1 and d_p=20 nm, the deposition ratio decreases from 0.59 to 0.56 with a rise of N_{E1} from 1 to 50. Nevertheless, further reduction of this parameter leads to a decrease of less than 0.01 in the deposition ratio. This phenomenon also exists for particles with a diameter of 70 nm when it reaches to N_{E1}=100. Hence, it can be concluded that there are threshold values for the effect of the EDL force, in agreement with other studies in the literature [90].

The movement and deposition of nanoparticles are illustrated in Fig. 14. The moving nanoparticles are red, the deposited nanoparticles are blue, and the foam environment is gray.

4.3. Nanoparticle deposition in Berea sandstone

Berea sandstone has much lower porosity than the OCFs examined in the previous section and is representative of geometries in subsurface flow applications, for instance for EOR The geometry of Berea sandstone (red and blue show the solid and pore, respectively) and the computational mesh are shown in Fig. 15.

Fig. 16 illustrates the sandstone's velocity contours and streamlines. As depicted in this diagram, the application of a pressure gradient results in fluid flow with a velocity of 1.5 m/s in certain areas, owing to the rock's low porosity. However, in numerous locations, the flow remains stagnant or moves at least an order of magnitude slower. This demonstrates the more complex behavior of the Berea sandstone in contrast to previously examined geometries.

As before, 10,000 particles were injected into the system. The deposition ratio decreases with increasing nanoparticle diameter. For instance, when N_{DL}=10, and N_{E1}=50 the deposition ratio of nanoparticles with a 20, 50, and 70 nm diameter is 0.78, 0.73, and 0.47, respectively. Fig. 17 illustrates how the nanoparticles move and are deposited. As for the OCFs, the moving particles are shown in red, and the deposited nanoparticles in blue. Here we can see that a significant fraction of the particles has deposited at the late time. However, due to the low speed of the nanofluid flow in some areas of the pore, some particles are neither deposited nor removed from the environment.

The influence of N_{E1} and N_{DL} on the deposition ratio is similar to those of OCFs. The increase of N_{E1} from 1 to 100 when the N_{DL}=10, results in a drop in the deposition ratio of nanoparticles with a 70 nm diameter from 0.82 to 0.61. Moreover, the deposition ratio increases from 0.74 to about 0.78 by increasing N_{DL} from 5.1 to 25 when N_{E1}=50. The parameters N_{E1} and N_{DL} have limited effect, as shown in Fig. 18.

4.4. Discussion

This study has investigated the effects of nanoparticle diameter, surface potentials, and Debye-Huckel length (the size of the EDL) on nanoparticle deposition ratio in various geometries: a microchannel, three OCFs, and Berea sandstone. The effects of these parameters on particle behavior have also been considered in numerical and experimental studies. When comparing the outcomes of transport and deposition of nanoparticles in the specified geometries, it is important to consider the following factors:

1- In the microchannel, which has a less complex structure compared to Berea sandstone and OCFs, the deposition ratio of nanoparticles is less than one third of the deposition ratio seen in the aforementioned porous media.

2- Berea sandstone has a lower porosity in comparison to foams, resulting in increased complexity in the flow field. Some nanoparticles entered effectively stagnant regions of the pore space of Berea and were neither deposited nor swept out of the pore space.

Although nanoparticles exhibit varying behavior in diverse environments, the overall trend of the deposition ratio remains consistent across multiple parameters. In this section, the results of our study will be compared to previously published papers.

4.4.1. The effect of surface potentials

As stated in Eq. (14), $N_{E1} \propto (\psi_1^2 + \psi_2^2)$. Hence, as the surface potentials ψ_1 and ψ_2 rise, N_{E1} increases which enhances the repulsive electrostatic double-layer force. Increasing N_{E1} decreases the deposition ratio of nanoparticles. The trends of retention as a result of increasing surface potential were also studied by Sadeghi et al. [90] for virus particles in porous media and Seetha et al. [52] for deposition in a single pore. Moreover, Bai and Tien [91], frome column experiments, found a relation between the attachment efficiency of colloids (of micron-size) to surface potentials as $(\psi_1^2 + \psi_2^2)^{-0.3121}$. Hence, our results are qualitatively consistent with these published results.

4.4.2. The effect of double layer thickness

N_{DL} has an inverse relationship with the Debye-Huckel length (the strength of the EDL). The Debye-Huckel length rises with decreasing ionic strength. Hence, an increase in the ionic strength decreases the EDL force leading to the enhancement of nanoparticle deposition. As expected, our simulations showed that retention increases with N_{DL}. The deposition of clay particles as a function of solution ionic strength was investigated experimentally by Compere et al. [92]. The results are qualitatively consistent with our simulation. Moreover, the effect of solution ionic strength variations and the Debye-Huckel length on

particle deposition in porous media, was also investigated in other studies which are consistent with our study [52,91].

5. Conclusions and future directions

Nanoparticle deposition in a subsurface environment decreases the content of attainable material in the bulk fluid, increases surface roughness, and affects the flow of nanofluid. The effect of deposition and transport of nanoparticles at the large-scale depends on their behavior in the pore-scale, which we investigated in this paper. This study used a numerical solver based on the open-source library OpenFOAM to investigate the deposition and transport of nanoparticles in different porous media, including Berea sandstone and open-cell foams (OCFs) with different porosities. The Eulerian-Lagrangian method was utilized to study the effects of nanoparticle diameter, porosity, surface potential, and double layer thickness. It has been assumed that the nanofluid is dilute and the interaction between particles is disregarded. Hence, this study does not take into account the accumulation of particles. Furthermore, the study did not consider the detachment of particles from the solid surfaces. Given the assumption indicated above, the outcomes are as follows:

- Higher porosity leads to lower retention. For instance, the deposition ratio of nanoparticles with 20 nm diameter in the foam with 80 % porosity is about 0.1 more than the foam with 90 % porosity.
- Brownian motion is significant: the random movement of particles allows them to encounter the solid walls, which otherwise they would avoid as close to the solid the flow is stagnant. Hence, nanoparticle attachment decreases with nanoparticle diameter and becomes negligible for diameters around 100 nm and greater.
- With an increase in N_{DL}, the diffuse double layer around two surfaces (particle and solid surface) become thinner. Hence the EDL repulsive force becomes smaller, enhancing nanoparticle retention. The interaction of nanoparticles with solid surfaces is made more repulsive by an increase in N_{E1}.Hence, the attachment of nanoparticles decreases. Beyond a threshold nanoparticle diameter, there is little retention, and varying N_{DL} and N_{E1} have little effect on the behavior.

The significance of this work is that the amount of deposition can now be quantified in complex three-dimensional porous media. The simulations can therefore be used as a platform to predict the filtration behavior of nanoparticle transport and to design porous media and the flow regime to either enhance or suppress retention as required, for a variety of applications.

Based on the aforementioned situations, this research can be used as a foundation for further investigations into the behavior of nanofluid flow in porous media. By incorporating features such as nanoparticle aggregation, accumulation, desorption, and other similar scenarios that were previously overlooked due to the dilution of the nanofluid or simplification of the model, the proposed model can be enhanced.

In future work, the code could be extended to multiphase flow and a range of other porous media, potentially with different surface interactions. We could consider deposition rates under steady-state conditions and comparison with experimental results.

CRediT authorship contribution statement

Milad Ramezanpour: Methodology, Software, Validation, Visualization, Writing – original draft. **Majid Siavashi:** Conceptualization, Data curation, Project administration, Resources, Supervision, Writing – review & editing. **Hamidreza Khoshtarash:** Formal analysis, Methodology, Software, Visualization, Writing – review & editing. **Martin J. Blunt:** Formal analysis, Methodology, Software, Visualization, Writing – review & editing.

Declaration of competing interest

The authors declare that they have no known competing financial interests or personal relationships that could have appeared to influence the work reported in this paper.

Acknowledgment

The authors would like to acknowledge the financial support of the Iran National Science Foundation (INSF) [grant number: 8153].

References

[1] Said Z, et al. Recent advances on the fundamental physical phenomena behind stability, dynamic motion, thermophysical properties, heat transport, applications, and challenges of nanofluids. Phys Rep 2021.
[2] Sharma K, et al. Significance of geothermal viscosity for the magnetic fluid flow between co-rotating porous surfaces. Numer Heat Transf Part A: Applic 2023;84 (9):980–91.
[3] Vijay N, Sharma K. Dynamics of stagnation point flow of Maxwell nanofluid with combined heat and mass transfer effects: a numerical investigation. Int Commun Heat Mass Transf 2023;141:106545.
[4] Selimefendigil F, Öztop HF. Coupled effects of corrugation and rotation on the phase transition and thermal process in a vented cavity under MHD convection. J Energy Storage 2024;77:109925.
[5] Siavashi M, et al. A numerical analysis of the effects of nanofluid and porous media utilization on the performance of parabolic trough solar collectors. Sustain Energy Technol Assess 2021;45:101179.
[6] Hatamleh RI, et al. Simulation of nanofluid flow in a solar panel cooling system to investigate the panel's electrical-thermal efficiency with artificial neural network. J Taiwan Inst Chem Eng 2023;104879.
[7] Tahmasbi M, et al. Thermal and electrical efficiencies enhancement of a solar photovoltaic-thermal/air system (PVT/air) using metal foams. J Taiwan Inst Chem Eng 2021;124:276–89.
[8] Selimefendigil F, Öztop HF. Multijet impingement heat transfer under the combined effects of encapsulated-PCM and inclined magnetic field during nanoliquid convection. Int J Heat Mass Transf 2023;203:123764.
[9] Selimefendigil F, Öztop HF. Thermal and phase change process in a branching T-channel under active magnetic field and two rotating inner cylinders: analysis and predictions by radial basis neural networks. Int J Heat Mass Transf 2023;217: 124548.
[10] Ram D, et al. Progression of blood-borne viruses through bloodstream: a comparative mathematical study. Comput Methods Programs Biomed 2023;232: 107425.
[11] Abbas F, et al. Nanofluid: potential evaluation in automotive radiator. J Mol Liq 2020;297:112014.
[12] Ramezanpour M, Siavashi M. Application of SiO 2–water nanofluid to enhance oil recovery. J Therm Anal Calorim 2019;135(1):565–80.
[13] Selem AM, et al. Pore-scale processes in tertiary low salinity waterflooding in a carbonate rock: micro-dispersions, water film growth, and wettability change. J Colloid Interface Sci 2022;628:486–98.
[14] Foroozesh J, Kumar S. Nanoparticles behaviors in porous media: application to enhanced oil recovery. J Mol Liq 2020;113876.
[15] Zhong X, et al. A state-of-the-art review of nanoparticle applications with a focus on heavy oil viscosity reduction. J Mol Liq 2021;344:117845.
[16] Suk H, et al. A new analytical model for transport of multiple contaminants considering remediation of both NAPL source and downgradient contaminant plume in groundwater. Adv Water Resour 2022;167:104290.
[17] Cohen A, et al. Coupled dissolution-precipitation reactions as a potential method for mitigating contaminant transport in carbonate aquifers. Adv Water Resour 2021;157:104052.
[18] Pak T, et al. Pore-scale investigation of the use of reactive nanoparticles for in situ remediation of contaminated groundwater source. Proc Natl Acad Sci 2020;117 (24):13366–73.
[19] Sun Y, et al. Properties of nanofluids and their applications in enhanced oil recovery: a comprehensive review. Energy Fuels 2020;34(2):1202–18.
[20] Raoof A, et al. PoreFlow: a complex pore-network model for simulation of reactive transport in variably saturated porous media. Comput Geosci 2013;61:160–74.
[21] Wang Z, et al. Mass transfer during surfactant-enhanced DNAPL remediation: pore-scale experiments and new correlation. J Hydrol 2023;621:129586.
[22] Kuang W, et al. Nanofluid-induced wettability gradient and imbibition enhancement in natural porous media: a pore-scale experimental investigation. Transp Porous Media 2020;134(3):593–619.
[23] Zhang B, et al. Pore-scale experimental investigation of oil recovery enhancement in oil-wet carbonates using carbonaceous nanofluids. Sci Rep 2020;10(1):1–16.
[24] Pak T, et al. The dynamics of nanoparticle-enhanced fluid displacement in porous media-a pore-scale study. Sci Rep 2018;8(1):1–10.
[25] Mobaraki S, et al. An experimental study on the mechanisms of enhancing oil recovery by nanoparticles-assisted surfactant flood. Geosyst Eng 2020;23(6): 315–31.
[26] Qin T, et al. Nanoparticle-stabilized microemulsions for enhanced oil recovery from heterogeneous rocks. Fuel 2020;274:117830.

[27] Alcorn ZP, et al. Pore-and core-scale insights of nanoparticle-stabilized foam for CO2-enhanced oil recovery. Nanomaterials 1917;10(10):2020.
[28] Tzachristas A, et al. The effect of surface wettability on calcium carbonate precipitation in packed beds. Surf Interfaces 2022;34:102354.
[29] Molnar IL, et al. Quantified pore-scale nanoparticle transport in porous media and the implications for colloid filtration theory. Langmuir 2016;32(31):7841–53.
[30] Chatterjee J, Gupta SK. An agglomeration-based model for colloid filtration. Environ Sci Technol 2009;43(10):3694–9.
[31] Molnar IL, et al. The impact of immobile zones on the transport and retention of nanoparticles in porous media. Water Resour Res 2015;51(11):8973–94.
[32] Molnar IL, et al. Predicting colloid transport through saturated porous media: a critical review. Water Resour Res 2015;51(9):6804–45.
[33] Shirbani M, et al. Improved thermal energy storage with metal foam enhanced phase change materials considering various pore arrangements: a pore-scale parallel lattice Boltzmann solution. J Energy Storage 2022;52:104744.
[34] Hosseini M, et al. Reliability assessment of the Lattice-Boltzmann Method for modeling and quantification of hydrological attributes of porous media from microtomography images. Adv Water Resour 2023;171:104351.
[35] Ashorynejad HR, Javaherdeh K. Investigation of a waveform cathode channel on the performance of a PEM fuel cell by means of a pore-scale multi-component lattice Boltzmann method. J Taiwan Inst Chem Eng 2016;66:126–36.
[36] Zhang C, et al. Solute transport in porous media studied by lattice Boltzmann simulations at pore scale and x-ray tomography experiments. Phys Rev E 2019;100 (6):063110.
[37] Parvan A, et al. Insight into particle retention and clogging in porous media; a pore scale study using lattice Boltzmann method. Adv Water Resour 2020;138:103530.
[38] Aslannejad H, et al. Application of machine learning in colloids transport in porous media studies: lattice Boltzmann simulation results as training data. Chem Eng Sci 2022;253:117548.
[39] Yan L, et al. A quantitative study of salinity effect on water diffusion in n-alkane phases: from pore-scale experiments to molecular dynamic simulation. Fuel 2022; 324:124716.
[40] Icardi M, et al. On the predictivity of pore-scale simulations: estimating uncertainties with multilevel Monte Carlo. Adv Water Resour 2016;95:46–60.
[41] Beaudoin A, et al. Numerical Monte Carlo analysis of the influence of pore-scale dispersion on macrodispersion in 2-D heterogeneous porous media. Water Resour Res 2010;46(12).
[42] Elimelech M. Particle deposition on ideal collectors from dilute flowing suspensions: mathematical formulation, numerical solution, and simulations. Separ Technol 1994;4(4):186–212.
[43] Irfan M. Study of Brownian motion and thermophoretic diffusion on non-linear mixed convection flow of Carreau nanofluid subject to variable properties. Surf Interfaces 2021;23:100926.
[44] Ding D, et al. Modeling bimolecular reactions and transport in porous media via particle tracking. Adv Water Resour 2013;53:56–65.
[45] Paster A, et al. Particle tracking and the diffusion-reaction equation. Water Resour Res 2013;49(1):1–6.
[46] Darbari B, Ayani MB. Heat transfer and deposition analysis of CuO-Water nanofluid inside a baffled channel: two-phase Eulerian–Lagrangian method. J Taiwan Inst Chem Eng 2023;104827.
[47] Vijay N, Sharma K. Magnetohydrodynamic hybrid nanofluid flow over a decelerating rotating disk with Soret and Dufour effects. Multidiscipl Model Mater Struct 2023;19(2):253–76.
[48] Dehghan P, et al. Computational fluid dynamic analysis of graphene oxide/water nanofluid heat transfer over a double backward-facing microchannel. J Taiwan Inst Chem Eng 2023;145:104821.
[49] Sunil, et al. Effect of thermal radiation on Bodewadt flow in the presence of porous medium. Pramana 2023;97(1):16.
[50] Sharma K, et al. Convective MHD fluid flow over stretchable rotating disks with dufour and Soret effects. Int J Appl Comput Math 2022;8(4):159.
[51] Sarvar-Ardeh S, et al. Hybrid nanofluids with temperature-dependent properties for use in double-layered microchannel heat sink; hydrothermal investigation. J Taiwan Inst Chem Eng 2021;124:53–62.
[52] Seetha N, et al. Correlation equations for average deposition rate coefficients of nanoparticles in a cylindrical pore. Water Resour Res 2015;51(10):8034–59.
[53] Khoshtarash H, et al. Pore-scale analysis of two-phase nanofluid flow and heat transfer in open-cell metal foams considering Brownian motion. Appl Therm Eng 2023;221:119847.
[54] Mahian O, et al. Recent advances in modeling and simulation of nanofluid flows-Part I: fundamentals and theory. Phys Rep 2019;790:1–48.
[55] Nayinian SMM, et al. Two phase analysis of heat transfer and dispersion of nano particles in a microchannel. presented at. In: the Heat Transfer Summer Conference; 2008. p. 457–63. vol. 48487.
[56] Afshar H, et al. Microchannel heat transfer and dispersion of nanoparticles in slip flow regime with constant heat flux. Int Commun Heat Mass Transf 2009;36(10): 1060–6.
[57] Andarwa S, et al. Effect of correcting near-wall forces on nanoparticle transport in a microchannel. Particuology 2014;16:84–90.
[58] Andarwa S, Tabrizi HB. Nanoparticle deposition in transient gaseous microchannel flow considering hindered motion and rarefaction effect. Korean J Chem Eng 2017; 34(5):1319–27.
[59] Sharaf OZ, et al. Numerical investigation of nanofluid particle migration and convective heat transfer in microchannels using an Eulerian–Lagrangian approach. J Fluid Mech 2019;878:62–97.
[60] Sadeghnejad S, et al. Numerical simulation of particle retention mechanisms at the sub-pore scale. Transp Porous Media 2022;145(1):127–51.
[61] Ramezanpour M, et al. Pore-scale simulation of nanoparticle transport and deposition in a microchannel using a Lagrangian approach. J Mol Liq 2022;355: 118948.
[62] Baruah JS, et al. Melting and energy storage characteristics of macro-encapsulated PCM-metal foam system. Int J Heat Mass Transf 2022;182:121993. https://doi.org/10.1016/j.ijheatmasstransfer.2021.121993 [Online]. Available:.
[63] Guo J, et al. Compression effect of metal foam on melting phase change in a shell-and-tube unit. Appl Therm Eng 2022;206:118124. https://doi.org/10.1016/j.applthermaleng.2022.118124 [Online]. Available:.
[64] Jadhav PH, N G. Optimum design of heat exchanging device for efficient heat absorption using high porosity metal foams. Int Commun Heat Mass Transf 2021; 126:105475. https://doi.org/10.1016/j.icheatmasstransfer.2021.105475 [Online]. Available:.
[65] Samudre P, Kailas SV. Thermal performance enhancement in open-pore metal foam and foam-fin heat sinks for electronics cooling. Appl Therm Eng 2022;205:117885. https://doi.org/10.1016/j.applthermaleng.2021.117885 [Online]. Available:.
[66] Dukhan N, Hmad AA. Thermal management of fuel-cell stacks using air flow in open-cell metal foam. Int J Therm Sci 2022;172:107370. https://doi.org/10.1016/j.ijthermalsci.2021.107370 [Online]Available:.
[67] Valizade M, et al. Experimental study of the thermal behavior of direct absorption parabolic trough collector by applying copper metal foam as volumetric solar absorption. Renew Energy 2020;145:261–9. https://doi.org/10.1016/j.renene.2019.05.112 [Online]. Available.
[68] Italiano C, et al. Silicon carbide and alumina open-cell foams activated by Ni/CeO2-ZrO2 catalyst for CO2 methanation in a heat-exchanger reactor. Chem Eng J 2022;434:134685. https://doi.org/10.1016/j.cej.2022.134685 [Online]. Available:.
[69] Kopanidis A, et al. 3D numerical simulation of flow and conjugate heat transfer through a pore scale model of high porosity open cell metal foam. Int J Heat Mass Transf 2010;53(11–12):2539–50.
[70] Wejrzanowski T, et al. Structure of foams modeled by Laguerre–Voronoi tessellations. Comput Mater Sci 2013;67:216–21.
[71] Falco S, et al. Generation of 3D polycrystalline microstructures with a conditioned Laguerre-Voronoi tessellation technique. Comput Mater Sci 2017;136:20–8.
[72] Sepehri E, Siavashi M. Pore-scale direct numerical simulation of fluid dynamics, conduction and convection heat transfer in open-cell Voronoi porous foams. Int Commun Heat Mass Transf 2022;137:106274.
[73] Paknahad R, et al. Pore-scale fluid flow and conjugate heat transfer study in high porosity Voronoi metal foams using multi-relaxation-time regularized lattice Boltzmann (MRT-RLB) method. Int Commun Heat Mass Transf 2023;141:106607.
[74] Dong H, Blunt MJ. Pore-network extraction from micro-computerized-tomography images. Phys Rev E 2009;80(3):036307.
[75] Blunt MJ. Multiphase flow in permeable media: a pore-scale perspective. Cambridge University Press; 2017.
[76] Marshall J, Li S. Adhesive particle flow: a discrete element approach, 36. New York: 35 Cambridge University Press; 2014. p. 37.
[77] J. Buongiorno, 'Convective transport in nanofluids', 2006.
[78] Savithiri S, et al. Scaling analysis for the investigation of slip mechanisms in nanofluids. Nanoscale Res Lett 2011;6:1–15.
[79] Li A, Ahmadi G. Dispersion and deposition of spherical particles from point sources in a turbulent channel flow. Aerosol Sci Technol 1992;16(4):209–26.
[80] Abouali O, et al. Three-dimensional simulation of Brownian motion of nano-particles in aerodynamic lenses. Aerosol Sci Technol 2009;43(3):205–15.
[81] Kim JH, et al. Slip correction measurements of certified PSL nanoparticles using a nanometer differential mobility analyzer (nano-DMA) for Knudsen number from 0.5 to 83′. J Res Natl Inst Stand Technol 2005;110(1):31.
[82] Akhatov I, et al. Aerosol focusing in micro-capillaries: theory and experiment. J Aerosol Sci 2008;39(8):691–709.
[83] Particle deposition and aggregation: measurement, modelling and simulation. Butterworth-Heinemann; 2013.
[84] Israelachvili JN. Intermolecular and surface forces. Academic Press; 2011.
[85] Huang P, et al. The effects of hindered mobility and depletion of particles in near-wall shear flows and the implications for nanovelocimetry. J Fluid Mech 2009;637: 241–65.
[86] Butt HJ, Kappl M. Surface and interfacial forces. John Wiley & Sons; 2018.
[87] Rajagopalan R, Kim JS. Adsorption of brownian particles in the presence of potential barriers: effect of different modes of double-layer interaction. J Colloid Interface Sci 1981;83(2):428–48. https://doi.org/10.1016/0021-9797(81)90339-8 [Online]. Available:.
[88] Fernandes C, et al. Validation of the CFD-DPM solver DPMFoam in OpenFOAM® through analytical, numerical and experimental comparisons. Granul Matter 2018; 20(4):1–18.
[89] Ounis H, et al. Brownian particle deposition in a directly simulated turbulent channel flow. Phys Fluids A: Fluid Dynam 1993;5(6):1427–32.
[90] Sadeghi G, et al. Systematic study of effects of pH and ionic strength on attachment of phage PRD1. Groundwater 2011;49(1):12–9.
[91] Bai R, Tien C. Particle deposition under unfavorable surface interactions. J Colloid Interface Sci 1999;218(2):488–99.
[92] Compère F, et al. Transport and retention of clay particles in saturated porous media. Influence of ionic strength and pore velocity. J Contam Hydrol 2001;49 (1–2):1–21.